Boosting the performance and durability of Ni/YSZ cathode for hydrogen production at high current densities via decoration with nano-sized electrocatalysts

Ovtar, Simona; Tong, Xiaofeng; Bentzen, Janet J.; Thydén, Karl T. S.; Simonsen, Søren Bredmose; Chen, Ming

Published in:
Nanoscale

Link to article, DOI:
10.1039/c8nr07678b

Publication date:
2019

Document Version
Peer reviewed version

Boosting performance and durability of Ni/YSZ cathode for hydrogen production at high current densities via decoration with nano-sized electrocatalysts

Simona Ovtar,† Xiaofeng Tong, Janet J. Bentzen, Karl T. S. Thydén, Søren Bredmose Simonsen and Ming Chen*

Conventional Ni/yttria stabilized zirconia (YSZ) electrodes in solid oxide cells experience fast degradation when operated for electrolysis of steam at high current densities. This study shows a relatively simple procedure of infiltrating $Ce_{0.8}Gd_{0.2}O_{2-\delta}$ (CGO) nanoparticles into the Ni/YSZ electrode to achieve stable cell performance. The long-term durability tests of the cells with a bare Ni/YSZ electrode and with a CGO infiltrated Ni/YSZ electrode were performed at 800 °C and -1.25 A/cm^2. The cell stability was followed by measuring cell voltage and recording electro-chemical impedance spectra. The post-mortem analysis of the tested cells was done with scanning and transmission electron microscopy. The CGO nanoparticles infiltration reduced the cell voltage degradation rate from 699 mV/kh for the bare Ni/YSZ electrode to 66 mV/kh for the infiltrated one. The investigation showed that after introducing CGO nanoparticles the steam reduction mechanism was changed and that the electrode degradation itself came from different mechanisms than for the bare Ni/YSZ electrode.

1. Introduction

Renewable energy sources like wind and solar are widely considered as the key technologies to cover our growing demands. However, the fluctuating nature of these sources requires a flexible energy system and storage technologies to ensure that energy supply can be covered in a stable and affordable manner [1]. Among the existing and under-development large-scale energy storage technologies, hydrogen storage in a form of pure hydrogen or other molecules produced by hydrogenation of carbon oxides, has high potential due to high energy density and easy integration into existing gas storage and gas distribution grids [2]. Hydrogen can be generated via electrolysis of water or steam and in this way, electricity can be chemically stored. In times of need, these fuels can be converted back to electricity by either conventional power plants or fuel cells.

Among the currently matured and upcoming technologies for water or steam electrolysis, solid oxide electrolysis cells (SOEC) have a low electricity demand, due to operation at high temperature (low equilibrium cell voltage) [3] and a relatively high stability against fluctuating and intermittent electricity sources. Even more, reduced degradation was reported when operating SOECs in reversible mode [4]. The key challenges for a successful commercialization of SOEC are the limited long-term stability and cost. The stability challenge is strongly correlated with the operation conditions of SOEC [5]. Nevertheless, to ensure a high production rate of hydrogen and to reduce investment costs (CAPEX), operation at high current densities (-1 A/cm^2 and higher) needs to be considered. For conventional solid oxide cells composed of a $La_{1-x}Sr_xMnO_{3-\delta}$ or $La_{1-x}Sr_xCo_{1-y}Fe_yO_{3-\delta}$ oxygen electrode, an yttria stabilized zirconia (YSZ) electrolyte and a Ni/YSZ fuel electrode the major degradation mechanisms at high-current steam electrolysis (above -1 A/cm^2) are delamination of the oxygen electrode, crack formation in the YSZ electrolyte, formation of ZrO_2 nano-particles on the Ni surface and bubbles in the YSZ electrolyte, destruction of the Ni-YSZ interface and poisoning of the Ni/YSZ electrodes with impurities [5–8]. The degradation of the Ni/YSZ electrode strongly depends on the cell's over-potential [5] or in other words the cathodic polarization. Under high cathodic polarization the Ni-YSZ interface undergoes severe disintegration including the reduction of Zr^{4+} and the formation of Ni-Zr alloys [9]. To the best knowledge of the authors, the conventional Ni/YSZ electrode has not demonstrated stable electrolysis operation at current density above -1 A/cm^2 for periods longer than a few thousand hours.

Currently, two strategies to improve the durability of the fuel electrodes are widely investigated; i) developing novel oxide-based electrodes with high electronic and ionic conductivity in reducing conditions and ii) introducing a better electro-catalyst into the Ni/YSZ electrode. For the first strategy a wide range of different perovskite materials have been studied [10], with a large focus on doped strontium titanates [11,12], doped strontium iron molybdates [13] and (La,Sr)(Cr,Mn)$O_{3-\delta}$ [14]. However, the catalytic activity of these perovskite-based electrode materials towards the steam splitting reactions is inferior to that of the Ni/YSZ electrode. For the later strategy, a relatively novel method of in-situ forming nano-sized electro-catalysts by solution infiltration in a porous structure is often used. The infiltration of electro-catalyst precursor solutions into a conventional solid oxide cell fuel electrode or oxygen electrode, or into a specially developed scaffold has shown to be very efficient in improving the electrode performance in the short term [8,15–19]. Whereas for long-term tests, only few operations of infiltrated electrodes tested in either fuel cell mode or electrolysis mode have been reported, focusing on oxygen electrode infiltration mainly [17,20–22].

The catalyst infiltration is a post-cell-production technique which requires several hundred degrees lower exposure temperature, and it is not limited to the match of thermal expansion coefficients (TEC) of the used materials. The infiltrated catalyst is formed as discrete nanoparticles supported by an electrode or a scaffold and thus the infiltration method allows implementation of a wide range of electro-

*Department of Energy Conversion and Storage, Technical University of Denmark, Frederiksborgvej 399, DK-4000 Roskilde, Denmark. *E-mail: minc@dtu.dk*
† OFS Fitel Denmark, Priorparken 680, 2605 Brøndbyvester, Denmark
Electronic Supplementary Information (ESI) available. See DOI: 10.1039/x0xx00000x

catalysts. For solid oxide fuel cell (SOFC) applications improved initial performance of the Ni/YSZ electrode has been demonstrated by infiltration of several different materials: tungsten bronzes [23], proton conductors [24,25], and mixed ionic and electronic conductors (e.g. doped-cerium oxide) [19,26–28], among which the infiltration of Sm- or Gd- doped cerium oxides (CSO or CGO) was most often reported.

The rare-earth doped cerium oxide infiltration of fuel electrodes got a large attention through considerable stability improvements of hydrocarbon SOFC [19,29], by eliminating carbon formation on the electrodes surfaces. A large increase of the activity of CGO or CSO infiltrated fuel electrodes of hydrogen SOFC has also been reported [27,30]. The infiltration process is in most cases done into a NiO/YSZ electrode that is afterwards reduced to Ni/YSZ. The reduction step drastically changes the microstructure of the electrode and can lead to encapsulation of catalysts and loss of percolation in the infiltrated layer. Therefore, the infiltration into a pre-reduced Ni/YSZ electrode can have several advantages compared to the NiO/YSZ electrodes including larger connected porosity (formed during reduction of NiO to Ni), control over preferential surfaces of infiltrated precipitation (Ni or YSZ grains) and exclusion of drastic microstructural change between infiltration step and operation of the cells. The CGO infiltration into pre-reduced Ni/YSZ electrodes has been already demonstrated on stack level, where surprisingly, the infiltration of a CGO-Ni composite into pre-tested Ni/YSZ electrodes of a SOFC stack showed almost no performance improvement [31]. On the other hand, a large performance improvement of CGO infiltrated Ni/YSZ electrodes of SOEC stacks, after operating the stacks for several hundred hours in CO_2-steam electrolysis, has shown that the CGO infiltration can be a useful tool for restoration of the fuel electrodes [32]. A different involvement of the CGO electro-catalyst in SOFC than in SOEC operation can describe the reported differences. For the hydrogen SOFC it has been reported that the presence of doped ceria in the fuel electrode, due to its high electronic and ionic conductivity, changes the hydrogen oxidation reaction site from a three phase boundary (e.g. Ni-YSZ-gas) to the entire surface of ceria [33] and thereby accelerates the hydrogen oxidation reaction. While, for a steam electrolysis the importance of the CeO_2-Ni interface as a steam reduction site was demonstrated by various experiments [34–36].

In the here reported study the main focus is on the catalytic effect of CGO nano-particles in high current density steam electrolysis and their influence on the steam reduction mechanism and electrode degradation mechanisms. The performance of the CGO infiltrated electrode SOEC was, on cell level, directly compared to the conventional SOEC operated at the same conditions and the steam splitting mechanism in the CGO nanoparticles infiltrated electrode was discussed in detail. With the CGO nano-particles infiltration the performance and stability issue of the conventional fuel electrodes operating at high current densities were addressed and mitigated. The improved catalytic activity of the CGO infiltrated fuel electrode resulted in a colossal improvement of the cell stability at high current densities compared to the conventional one and minor degradation rates were achieved. We proposed that the catalytic CGO nano-particles can increase the steam splitting rate and reduce the local over-potential at the electrode and thereby reduce a hazard of the electrode degradation.

2. Experimental

2.1 Cell info

The cells tested in this work were Ni/YSZ fuel electrode supported SOECs manufactured from the same production batch. The cells consist of a Ni/YSZ support (~300 μm in thickness), a Ni/YSZ fuel electrode (~10 μm in thickness), an YSZ electrolyte (~8 μm in thickness), a CGO10 ($Ce_{0.9}Gd_{0.1}O_{1.95}$) inter-diffusion barrier layer (~5 μm in thickness) and a LSCF/CGO (LSCF: $La_{0.6}Sr_{0.4}Co_{0.2}Fe_{0.8}O_{3-\delta}$) oxygen electrode (~25 μm in thickness)[37]. The cells had a foot print of 5.3 × 5.3 cm^2 and an active electrode area of 4 × 4 cm^2.

2.2 Testing

The setup for single cell testing was illustrated and described in detail previously [38,39]. In this work, a gold seal was used to seal the fuel electrode gas flow compartment whereas no seal was used for the oxygen electrode side. Corrugated gold and nickel meshes as gas distribution layers and gold and nickel plates as current collector components were used on the oxygen and fuel electrode side, respectively. To ensure gas tight sealants and electrical contact between the cell and the contact components, four kilograms of weight was applied on top of the cell house during start up and throughout the test.

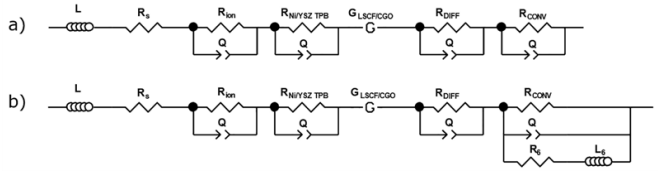

For reduction, all the cells were heated (1 °C/min) to 850 °C and the fuel electrode was reduced first in 9 % H_2 in Ar for 2 h, followed by another 2 h reduction in H_2 with 4 % steam. One cell, hereafter named as Cell A, was then continued for electrochemical performance characterization and long-term durability test at 800 °C. Two other cells (Cell B1 and Cell B2) were brought to room temperature in the cell test house and were afterwards infiltrated with CGO on the reduced Ni/YSZ electrode side. The infiltration procedure will be presented in detail in the following section 2.3. After infiltration, Cells B1 and Cell B2 were mounted again into the cell house and were heated to 800 °C for characterization and durability tests.

The electrochemical performance of the cells was characterized at 800 °C both before and after the long-term durability test. DC polarization (*iV*) curves and AC electrochemical impedance (EIS) measurements were carried out, with 50 l/h air or pure oxygen supplied to the oxygen electrode and 24 l/h of H_2 with 4 %, 20 %, or 50 % of steam to the fuel electrode. The long-term durability test was conducted at 800 °C and -1.25 A/cm^2, with 50 l/h of pure oxygen supplied to the oxygen electrode and H_2O/H_2 (90/10) to the fuel electrode. For Cell A and Cell B1 13.4 l/h of H_2O + H_2 (H_2O/H_2 = 90/10) was supplied to the fuel electrode and for Cell B2 22 l/h of H_2O + H_2 (H_2O/H_2 = 90/10) to the fuel electrode, resulting in a steam conversion of 70 % and 42 % at -1.25 A/cm^2, respectively. A Solartron 1255 frequency analyzer was used for

recording EIS both at OCV and under current. EIS were recorded with 12 points/decade in a frequency range from 82451 to 0.08 Hz and were corrected using the short circuit impedance response of the test setup.

In this work, EIS are presented in Nyquist plots. Furthermore, plots of distributions of relaxation times (DRT) [40] and analyses of difference in impedance spectra (ADIS) [41] are provided. The DRT plots are used to illustrate the development of impedance over time and to highlight frequency ranges for different processes contributing to the total impedance response of the cells. To quantitatively break down losses, a complex-non-linear-least-squares (CNLS) method was used to fit an equivalent circuit model shown in Figure 1 to the measured EIS data. The model shown in Figure 1a was adopted from a reported model used for the same types of Ni/YSZ electrode supported SOEC cells [39], and was employed in the current work to model EIS at OCV for all the three cells and the EIS of Cell B1 and Cell B2 under current. In this model, $(RQ)_{ion}$ corresponds to the high frequency arc at ~10-40 kHz and accounts for the ionic transport process through the ionic conducting matrix in the electrodes. The R_{ion} can be expected for the here studied cell to originate mainly from the Ni/YSZ electrode, but not from the mixed ionic electronic conducting LSCF/CGO oxygen electrode [42]. The $(RQ)_{Ni/YSZ\ TPB}$ at ~1-4 kHz is ascribed to the electrochemical process at the triple phase boundaries (TPBs) of the Ni/YSZ electrode. The impedance response from the LSCF/CGO oxygen electrode at a characteristic frequency of ~100 Hz is approximated by a Gerisher element. The gas diffusion and the gas conversion were approximated by two RQ-circuits at characteristic frequencies around ~40 Hz and ~2 Hz, respectively [43,44]. The EIS data measured under current load for Cell A were fitted by the equivalent model shown in Figure 1b. The model was developed by combining the model in Figure 1a with the model proposed for the Ni/YSZ model electrodes operating at high cathodic polarizations [9]. The R_6L_6 was added to describe the inductance loop observed at low frequency in the measured EIS of Cell A under high current load, as explained in Section 3.2.1. All analysis was performed using the in-house developed RavDav software package [45].

Figure 1: The equivalent circuit model used to fit the measured data of impedance spectra: a) for data of Cell A measured under OCV and data of Cell B1 and Cell B2, b) for data of Cell A measured under current load

2.3 Infiltration

The CGO ($Ge_{0.8}Gd_{0.2}O_{1.9}$) precursor solution was prepared by mixing Ce- and Gd- nitrates stock solutions in a molar ratio of 8 : 2 to obtain 0.3 mol/l solution. The Ce-nitrate and Gd-nitrate were supplied by Alfa Aesar. Comparing with other work of CGO infiltration[27,30], a surfactant PE-L62 (Sigma-Aldrich Corporation) with 1.4 wt. % per weight of solution was added to improve wetting of the structure. The CGO precursor solution with viscosity of 1.1 mPa·s was spread over the entire surface (5.3 x 5.3 cm^2) of the Ni/YSZ electrode. A high amount of the solution was ensured to completely fill the pores of the Ni/YSZ support and the Ni/YSZ electrode. The remained solution was removed from the surface prior placing the cell in a pre-heated furnace at 200 °C and heating it up to 300 °C with a rate of 5 °C/min. The cell was held at 300 °C for 12 min and then was cooled down to 200 °C. After that, the cell was taken out of the furnace and the infiltration step with a sequential heat treatment was repeated for several times to obtain a loading of 125 mg CGO per 1 cm^3 Ni-YSZ backbone (Ni/YSZ electrode + Ni/YSZ support). The infiltrated cells were then mounted into a single cell testing set-up, as described in Section 2.2.

2.4 Nanostructure and microstructure characterizations

Scanning electron microscopy (SEM, Carl Zeiss Supra 35 and Merlin) was used to study fractured surfaces and polished cross-sections of the as-prepared infiltrated and reduced reference cells and the cells A and B1 after long-term durability steam electrolysis tests. The cells were cut, embedded into epoxy resin, ground and polished or simply fractured to study the microstructure of the cell cross sections at different distances from the gas inlet and gas outlet. Images were taken at acceleration voltages from 15 kV to 2.5 kV with secondary and back-scattered electron detectors to investigate the microstructure and phase distribution, and at low acceleration voltage (0.95 kV) with an in-lens detector to investigate electron percolation in the Ni-YSZ structure [46].

Transmission electron microscopy (TEM) and scanning transmission electron microscopy (STEM) in combination with

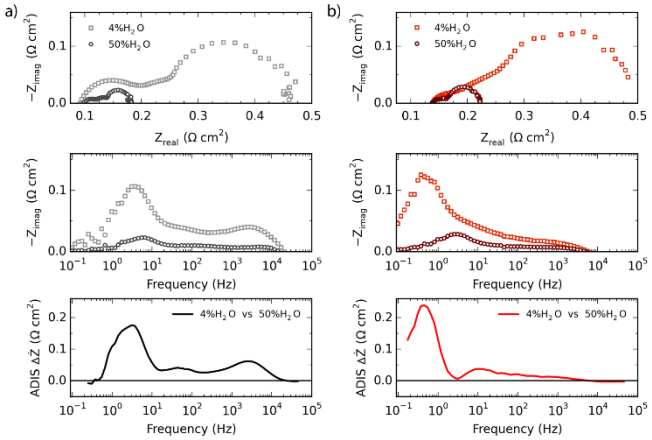

energy dispersive spectroscopy (EDS) were performed on cell B1 after long-term durability steam electrolysis tests by using a JEOL 3000F equipped with a field emission gun operated at 300 kV, a high annular angle dark field (HAADF) STEM detector, and an Oxford instruments EDS detector. The specimen was prepared for TEM and STEM by mechanically thinning and mounting on a Cu half ring followed by final thinning by using a Carl Zeiss Crossbeam 1540XB focused ion beam (FIB). The FIB thinning was performed with a 10 nA - 20 pA probe current and an acceleration voltage of 30 kV. Prior to thinning a ~400 nm thick protective layer of Pt was deposited on the surface of the sample by use of a gas injection system (GIS) and ion beam assisted deposition. For STEM-EDS analysis the specimen was tilted 21° towards the EDS detector to minimize absorption of low energy X-rays, a nominal probe size of 0.7 nm and a camera length of 12 cm was used. Quantifications of the EDS spectra were performed with calculated k-factors from the INCA software. High-resolution TEM (HRTEM) images recorded during the in-situ experiment were analyzed with the

CrystalMatch software[47]. Here at least three independent measurements, two lattice distances and the angle between the planes were compared to theoretical values described in crystallographic information files (CIF) of the following structures: Ni (F m -3 m), cubic NiO (F m -3 m), trigonal NiO_2 (R -3 m H), cubic $Zr_{0.8}Y_{0.2}O1.9$ (F m -3 m), tetragonal $Zr_{0.86}Y_{0.14}O_{1.93}$ (P 42/n m c S), tetragonal ZrO_2 (P 42/n m c Z), monoclinic ZrO_2 (P 1 21/c 1), cubic $Ce_{0.8}Gd_{0.2}O_{1.9}$ (F m -3 m), trigonal Ce_2O_3 (P 3 2 1), tetragonal $CeAlO_3$ (I 4/m c m), tetragonal $CeAlO_3$ (P 4/m m m). Crystals are found to be consistent with a structure if all three measurements agree with the theoretical values within estimated measurement errors of 10% for distances and 5% for angles.

3. Results

3.1 Electrochemical performance of cells

The SOEC performance degradation over several hundreds of hours observed as a cell voltage increase at the constant current density of -1.25 A/cm^2. The here studied cells showed large deviations in the degradation profiles. For the cell with a bare Ni/YSZ electrode (Cell A) the cell voltage increased with a rate of 699 mV/kh, which was several times larger than for the cells with the CGO infiltrated Ni/YSZ electrodes (Cell B1 and Cell B2) with a cell voltage increase rate of 66 mV/kh – 162 mV/kh. To demonstrate the differences and clarify the mechanisms behind, the following section is divided into three sub-sections: the performance at open-circuit voltage (OCV) (3.1.1), the performance under an applied current (3.1.2) and the long-term high current density steam electrolysis durability tests (3.1.3).

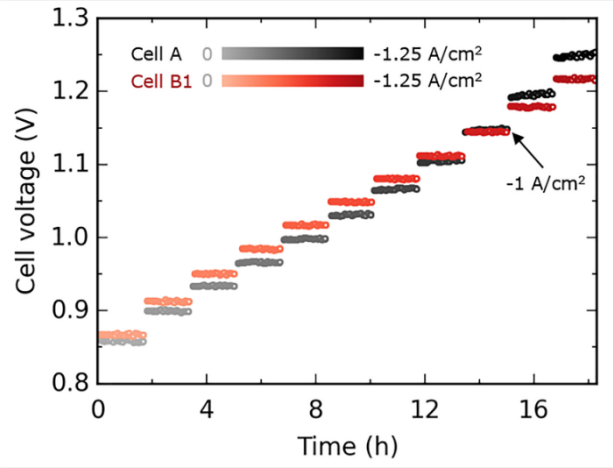

3.1.1 Performance under OCV

The EIS of the cells with a bare Ni/YSZ electrode (Cell A) and a CGO infiltrated Ni/YSZ electrode (Cell B1) measured at OCV are shown in Figure 2a-b. The estimated ohmic resistance (R_s), extracted from Figure 2 as the x-axis (Z_{real}) intercept of the EIS curve at high frequencies, was slightly lower for Cell A than for Cell B1. The measured difference in R_s can have several different origins; however, since R_s describes the oxygen ion transport in the bulk of the electrolyte and the electrode and the electron (electron hole) transport in the bulk of the electrodes, it is most likely that the R_s difference comes from the unequal contact between the cell-testing-setup and the cell. However, it cannot be completely ruled out that the difference in R_s origins from microstructural changes, e.g. weakening the electrode-electrolyte interface and damaging the oxygen contact layer-oxygen electrode interface. The estimated total polarization resistance (R_p), roughly speaking presented as two-three semicircular arcs in the Nyquist plot in Figure 2, of Cell A and Cell B1 seem to be very similar. This implies that the CGO infiltration does not have drastic influence on the R_p at OCV.

Figure 2: Recorded EIS measured during the initial characterization of a) Cell A, b) Cell B1 at different H_2O:H_2 ratios at the fuel electrode with the corresponding ADIS plots for the gas composition shifts

The impedance frequency ranges corresponding to the processes that are sensitive to the gas composition change occurring on the specific electrode have been identified by employing the ADIS on the recorded EIS of gas composition shift (the gas composition at one electrode was changed and at the other electrode was kept unaltered). The steam content change from 4 % (used as a reference in the ADIS pots) to 50 % in the fuel (H_2 + H_2O) resulted in a drastic change of the impedance (Figure 2). For Cell A (Figure 2a) the impedance decreased in three major frequency ranges; the low frequency range impedance (1 – 10 Hz), which can be ascribed to gas conversion process, the intermediate frequency range impedance (10 – 100 Hz), which can be ascribed to the gas diffusion process and the high frequency impedance (1 kHz – 10 kHz), which can ascribed to surface exchange process on the Ni/YSZ three-phase boundary (TPB) [41]. Contrary, for Cell B1 (Figure 2b) with the increased steam content in the fuel the impedance decreased only in two ranges: the low and the intermediate frequency range. The lack of sensitivity of the high frequency contributions to the change of the steam content suggested that the CGO infiltration influences the steam reduction mechanism on the Ni/YSZ TPB at OCV.

The gas composition shift for the oxygen electrode from air (21% O_2) to pure O_2 (presented in Supplementary information in Figure S1) resulted in a decreased impedance in two frequency ranges; a low frequency (from 1 – 10 Hz) and an intermediate frequency (0.1 – 1 kHz). The low frequency contribution is most probably correlated with the gas conversion resistance and the intermediate frequency impedance can be ascribed to the surface oxygen exchange process occurring at the oxygen electrode [41]. As expected from the fact that only the fuel electrode was modified in the here presented study, no significant difference in the oxygen electrode gas-composition-shift ADIS plots of Cell A and Cell B1 was observed.

3.1.2 Under applied current

During SOEC operation, steam splits to hydrogen and oxide ions at the fuel electrode, which are then transported through the electrolyte to the oxygen electrode, where the oxygen evolution occurs. A higher cell voltage at a constant current density means that Figure 3: The cell voltages of Cell A and Cell B1 versus time at

different applied constant current densities from 0 A/cm^2 to -1.25 A/cm^2 with the step of 0.125 A/cm^2.

Figure 4: The recorded EIS for a) Cell A and b) Cell B1 at different applied current densities from 0 A/cm^2 to -1.25 A/cm^2 with the step of 0.25 A/cm^2.

a larger input power is needed to generate the same amount of hydrogen. Figure 3 shows the cell voltages of Cell A and Cell B1 at constant applied current densities from 0 A/cm^2 to -1.25 A/cm^2. At low current densities the cell voltage of Cell A was lower than that of Cell B1, i.e. the cell with the bare Ni/YSZ electrode outperformed the cell with the CGO infiltrated electrode. At higher current densities (> -1 A/cm^2) the CGO infiltration showed to be highly beneficial and the cell voltage was substantially lower compared to the cell with the bare Ni/YSZ electrode.

In Figure 4 the EIS recorded at different current densities revealed that the observed difference in the cell voltage between Cell A and Cell B1 comes from the R_p contributions. For Cell A in the range of 0

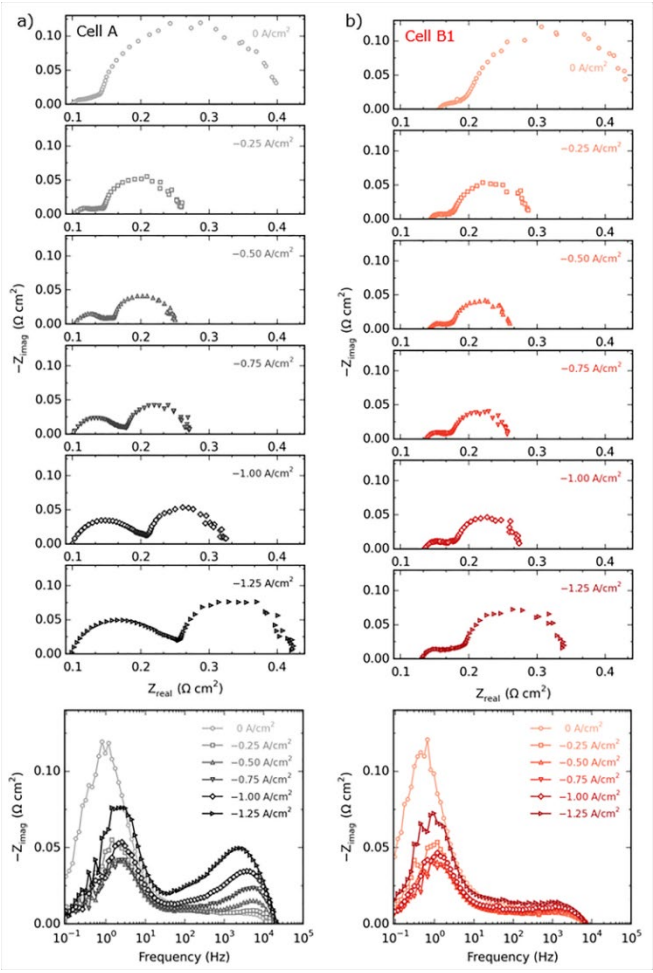

A/cm^2 to -0.75 A/cm^2 the high frequency R_p contribution was increasing with current density and the low frequency contribution was decreasing. At -1.25 A/cm^2 both contributions were increased compared to those at -0.75 A/cm^2. For Cell B1 the low frequency R_p contribution was also decreasing with increasing current density. At the same time, the high frequency contribution was much less sensitive to the increased current density compared to Cell A. The low frequency contribution, which was the dominating contribution and very similar for both cells, had a peak maximum at around 1 Hz and can be ascribed to a gas conversion process. Its change with current density is expected due to change in steam conversion and different local H_2O:H_2 ratios [48]. The high frequency contribution had a maximum peak at 2.2 kHz and can be ascribed to the Ni/YSZ TPB resistance ($R_{TPB,Ni}$). Its increase with the current density demonstrated that severe changes occurred at the fuel electrode of Cell A compared to the CGO infiltrated fuel electrode of Cell B1, where changes are expected to be minor.

Figure 5: Recorded EIS for a) Cell A and b) Cell B1 at 800 °C and -1.25 A/cm^2 (dotes) with the CNLS model fit (black line) and the semi-circles corresponding to specific processes at the cell. Relative residuals are included to show a good match between the recorded data and the fitted model. c) The resistances of cell A and Cell B1 extracted from the fits.

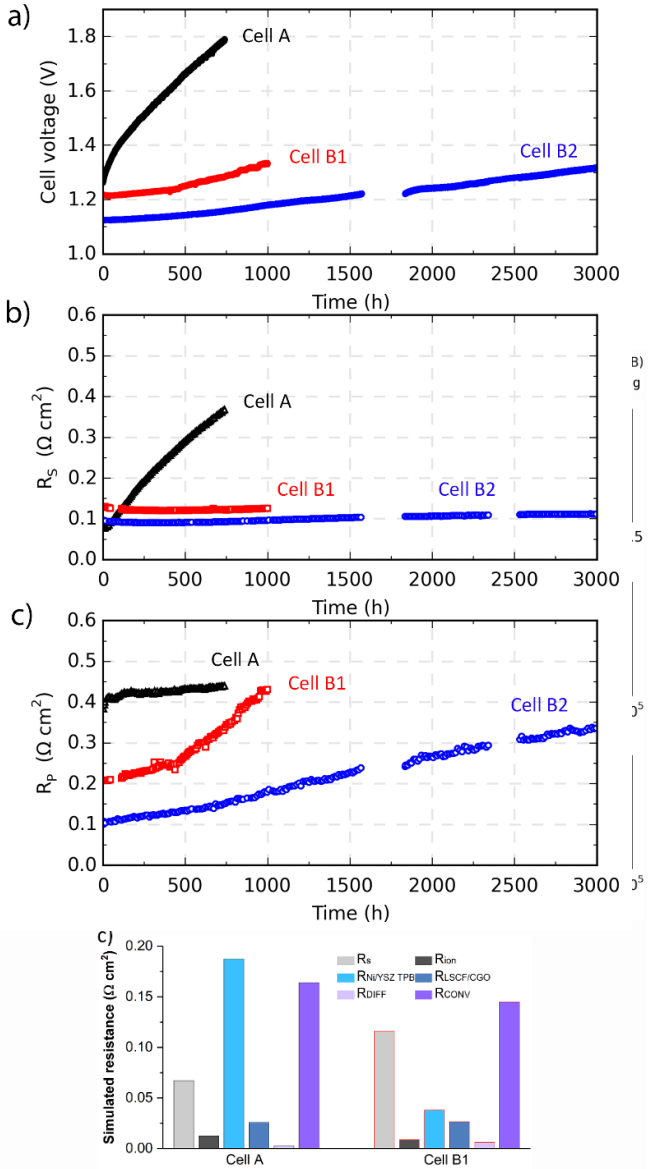

A fitting of the CNLS model (Figure 1a) to the recorded EIS, by implementing the findings from the gas shift experiment (Figure 2), resulted in a good match between the CNLS model and the measured EIS (a-b). The total polarization resistance of the cells at -1.25 A/cm^2 was split to contributions from five different processes (c). A large and very similar contribution of R_{Conv} was observed for both cells, which is well in line with the calculated R_{Conv} of 0.193 Ω cm^2 by the Plug-Flow model described in ref. [48]. Between Cell A and Cell B1, the

largest difference in the contribution to the total polarization resistance is found in $R_{TPB,Ni}$. Cell B1 had much smaller contributions of the $R_{Ni\text{-}TPB}$ than Cell A. The improvement can result from two facts: i) CGO has better intrinsic catalytic properties and ii) with the CGO infiltration, due to presence of nanoparticles, the surface area, where the steam splitting occurs, is significantly increased. The two cells differ also in R_{ion}, R_{DIFF}, and R_{CONV}, though to different degrees with regard to absolute and relative differences. For example, Cell B1 has a slightly larger R_{Diff} than Cell A, 0.003 Ω cm^2 as the absolute difference and 100 % as the relative change. On the contrary, R_{CONV} decreases after the CGO infiltration, -0.019 Ω cm^2 as the absolute difference and -11 % as the relative change. It is speculated that the infiltration of CGO nanoparticles clogs some of the gas channels and through this slows down the gas diffusion through the 300 μm thick Ni/YSZ porous support, hence increases R_{Diff}. The decrease of R_{CONV} could be due to the catalytic effect of CGO on the steam reduction reaction. However, taking the uncertainty of impedance analysis into account, further experiments are needed to consolidate the above speculation.

3.2 Long-term durability tests

Long-term durability tests under a current load of -1.25 A/cm^2 at 800 °C following the cell voltage development and the EIS development are shown in Figure 6. The cell performance degradation was evaluated as a rate of the cell voltage increase, the ohmic resistance increase and the polarization resistance increase (Figure 6). As mentioned in Section 3.1 and shown in Figure 6, a large difference between the cells with the bare Ni/YSZ electrode and the cells with the CGO infiltrated fuel electrode was observed, with the trend of a much faster degradation for the former. The cells were also tested under different steam conversion rates, Cell A and Cell B1 were tested under a steam conversion of 70 % and Cell B2 under a lower steam conversion of 42 %. The steam conversion had a large impact on the degradation rate of the cell performance and Cell B2 with larger amount of steam supplied to the fuel electrode showed lower degradation rate compared to Cell B1.

Cell A degraded fast through the entire testing period of 750 h with the cell voltage degradation rate of 0.699 V/kh, the average R_s degradation rate of 0.388 Ω·cm^2/kh, and the average R_p degradation rate of 0.075 Ω·cm^2/kh. The degradation of R_s can be ascribed to the Ni-YSZ conductivity changes[49,50]. The R_p degradation profile of Cell A can be split into two segments: the first 60 h and the following 690 h, since the degradation of Cell A had been significantly different in the first 60 h compared to the rest of the test. The EIS development of the first 60 h is shown in Figure 7a. At t = 0 h the polarization resistance can be roughly modelled with two semi circles. At t > 0 additional feature appears at low frequency range, which looks like a slightly suppressed full circle, and can be simulated by a low frequency arc coupled with an inductive loop, as shown by Hansen et al. [9] (and in the model in Figure 1b). The changed impedance at low frequency could origin from a severe reduction of the fuel electrode, that was observed by microstructural investigation of a cell operated at high current densities [5]. Besides, also the summit frequency of maximal $-Z_{imag}$ in high frequency range (0.2 – 1.1 kHz) was to a great extent decreased in the first 60 h, as shown in the DRT plot in Figure 7a. A similar decrease was reported for Ni/YSZ based solid oxide cells operated at lower current densities [42].

Following 690 h of electrolysis at high current densities the largest contribution to the cell degradation of Cell A came from the increased R_s, while the R_p was relatively stable (Figure 6). The imaginary part of the EIS, i.e. the polarization resistance, did not change significantly over time as shown in Figure 7b, where DRT curves are overlapping each other. The only change is observed at high frequencies (50 kHz), which corresponds to contributions from R_{ion} and which can be correlated to processes occurring at both electrodes. However, since a mixed ionic and electronic conducting oxygen electrode was used, a contribution from the oxygen electrode is less likely [51]. The increase of R_{ion} through the testing is

Figure 6: Galvanostatic long-term steam electrolysis durability tests under -1.25 A/cm^2 at 800 °C. a) Voltage development during time, b) ohmic resistance and c) polarization resistance development during time (extracted from EIS) of the cell with the bare Ni/YSZ electrode (Cell A), and the cells with the CGO infiltrated Ni/YSZ electrode (Cell B1 and Cell B2). Cell B2 was brought to OCV in 1573 – 1834 h. In 2341-2530 h no EIS measurements were performed though Cell B2 was still operated under -1.25 A/cm^2.

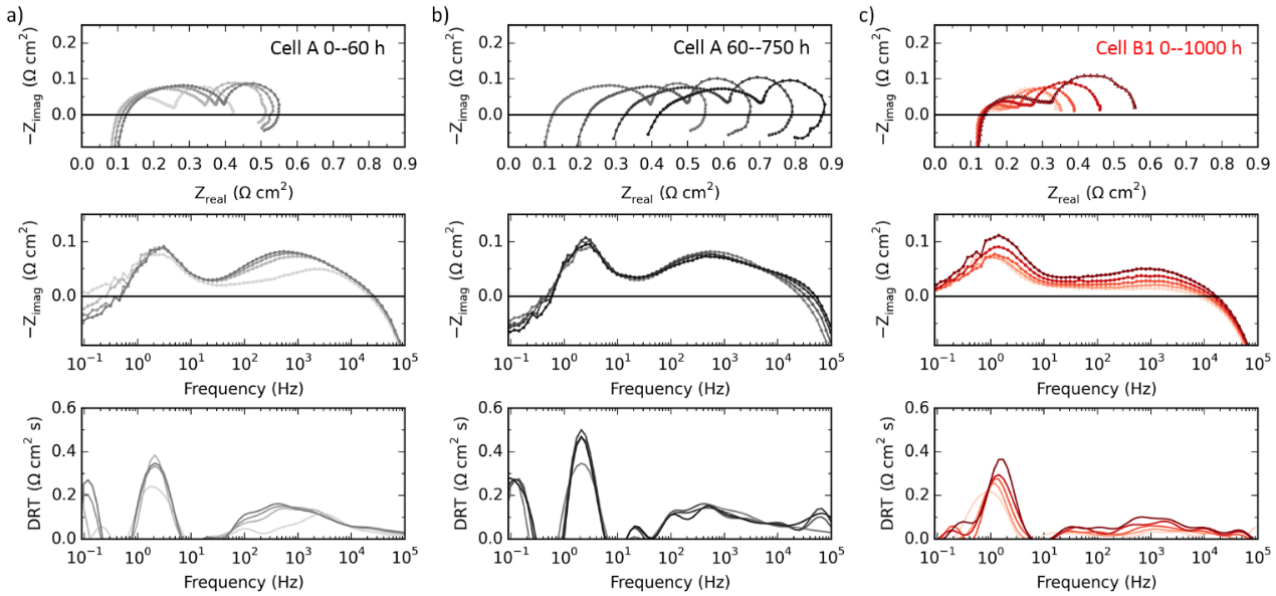

Figure 7: Recorded EIS and DRT plot of Cell A: a) the first 60 h of the electrolysis test (every 15 h) and b) the 60 h – 750 h of the test (every 230 h). c) Recorded EIS and DRT plot of Cell B1 of the 0 h – 1000 h (every 250 h). The testing time is presented as a change of color from bright (start) to dark (end).

most probably correlated to changes in electrodes ionic conducting matrix, for example in case of severe degradation of the electrode including the reduction of Zr^{4+} and precipitation of ZrO_2 nano-particles as reported by Chen et al. [5] for high current density steam electrolysis. The same degradation mechanism will also cause an increase of R_s by moving the steam splitting reaction site further away from the electrolyte and extending the oxide ion diffusion path.

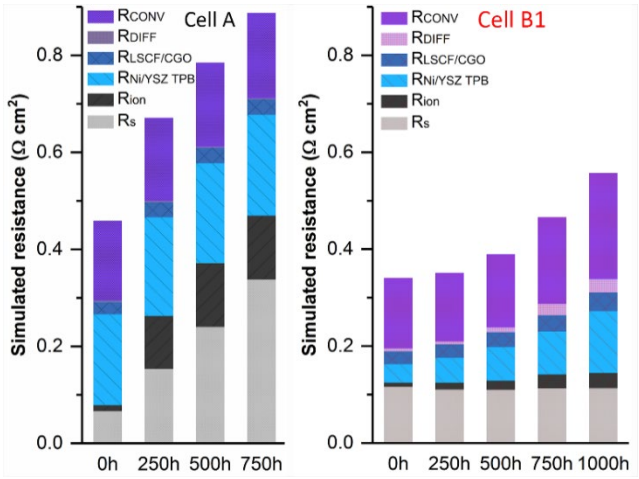

Figure 8: Development of the resistances of Cell A (with the bare Ni/YSZ electrode) and Cell B1 (with the CGO infiltrated Ni/YSZ electrode) extracted from the fits (in Figure S2 and Figure S3) during the durability test at the steam conversion of 70 %.

The cell voltage degradation rate of Cell B1 was much smaller compared to Cell A (Figure 6). Within the first 500 h of the operation, the cell voltage degraded with a rate of 66 mV/kh and afterwards with a rate of 162 mV/kh (the measured values are given in Table S1). The degradation of the Cell B1 performance was mainly due to the increase of R_p with an average rate of 224 mΩ·cm²/kh and the increased EIS at the intermediate frequency range of 1 kHz (Figure 7c), indicating a change in the steam splitting reaction sites. The R_s was stable through entire test (the rate of -5 mΩ·cm²/kh), which demonstrated that the conductive network didn't change during the operation.

The resistances obtained by fitting the measured impedance spectra during the durability test at -1.25 A/cm² (shown in Figure S3) with the equivalent circuit model described in Section 2.2 are shown in Figure 8 (the values are in Table S2). The largest differences between Cell A and Cell B1 are found in R_S, R_{ion}, $R_{Ni\text{-}TPB}$ and R_{Diff}, where the origin of change in R_S, R_{ion} and $R_{Ni\text{-}TPB}$ have been discussed above. The increase of R_{Diff} of Cell B1 during the durability test can be ascribed to sintering of the infiltrated CGO nanoparticles and through this reducing the gas diffusion channels. The sintering of the CGO nanoparticles is to be expected, due to the low synthesis temperature of 300 °C during the infiltration process.

Figure 9: Development of the resistances of Cell B2 (with the CGO

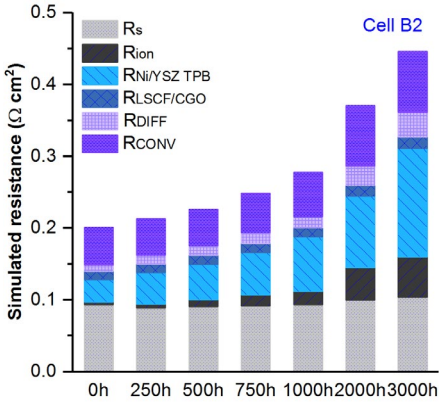

infiltrated Ni/YSZ electrode) extracted from the fits (in Figure S4) during the durability test at steam conversion of 42 %.

3.2.1 Lower steam conversion

The degradation rate of the CGO infiltrated cell was strongly dependent on the steam conversion rate at the fuel electrode. To reduce the steam conversion from 70 % for Cell B1 to 42 % for Cell

B2 and keep the same current density, the steam and hydrogen inlet flow rate (at constant H_2/H_2O ratio) were increased, which significantly reduced the degradation rate (Figure 6). For Cell B2, the average cell voltage degradation rate was 64 mV/kh, the average R_s degradation rate was 5 mΩ·cm^2/kh and the average R_p degradation rate was 77 mΩ·cm^2/kh for 3000 h of steam electrolysis. The results of fitting equivalent circuit model to the recorded EIS (Figure S4 and Table S4) revealed that also for Cell B2 (compared to Cell B1) the strongest contribution to the increased R_p came from the increase of $R_{Ni\text{-}TPB}$, as shown in Figure 9. The R_{ion} and R_{Diff} have also increased. However, with low steam conversion Cell B2 was outperforming Cell B1 even after 3-times longer testing time of 3000 h.

3.3 Change of microstructure

The microstructural changes of cells with a bare Ni/YSZ electrode after long-term electrolysis test at high current densities have been shown and in details described in our previous studies [5,52]. Briefly, under the here studied conditions (90/10 H_2O/H_2, 800 °C, -1.25 A/cm^2) three main changes of the microstructure have been observed: loss of contact between Ni-YSZ particles, loss of contact between Ni-Ni particles and Ni particle migration away from the electrolyte as shown in Supplementary Information (Figure S5a).

The microstructure of Cell B1's Ni/YSZ electrode after 1000 h long-term steam electrolysis durability test is shown in Figure 10 and Figure S5c,d. The microstructure is well in line with the microstructure of the Ni/YSZ electrode prior testing of the cell (for the microstructure of a parallel cell see Ref. [52] and Supplementary information Figure S5b). After 1000 h of testing, a slight deviation between the electron percolating Ni phase distribution at the gas inlet (Figure 10b) and at the gas outlet (Figure 10d) was observed. At the gas inlet less percolating Ni particles close to the electrolyte were found as compared to the gas outlet. The Ni migration at intermediate temperatures under cathodic polarization was speculated to origin from a loss of contact between YSZ-Ni particles and Ni-Ni particles, due to sintering or reshaping of Ni particles [52]. Consequently, some Ni particles are no longer part of the TPB where the steam reduction occurs and do not feel the cathodic polarization. The process of Ni migration is accelerated by a potential gradient, which is higher at the inlet than at the outlet.

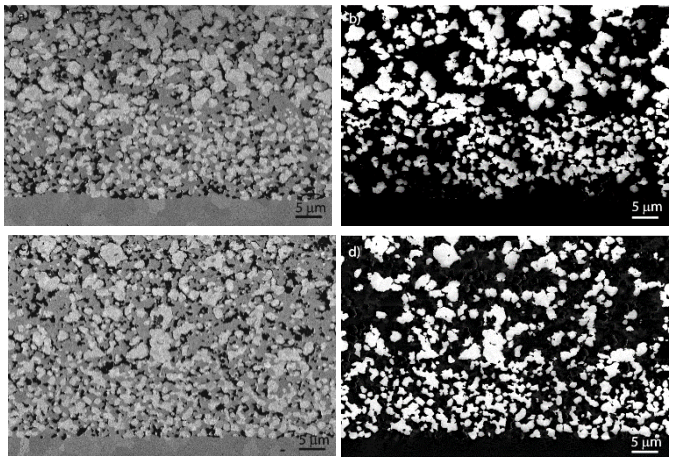

Figure 10: Microstructure of Cell's B1 fuel electrode after 1000 h of steam electrolysis at -1.25 A/cm^2 at 800 °C. a), b) at the gas inlet and c), d) at the gas outlet. b), d) Micrographs showing electron percolating Ni.

Figure 11: Micrographs of fractures surface of the CGO infiltrated Ni/YSZ electrode (Cell B1) a) before testing and b) after1000 h test under -1.25 A/cm^2. Ellipse – CGO layer on YSZ particles, Square – Ce-containing layer on Ni particles.

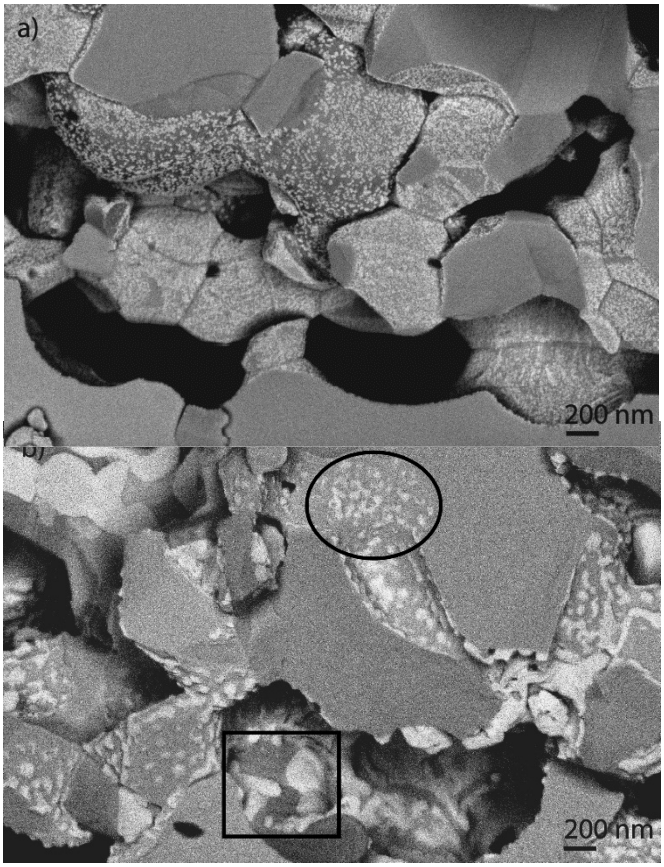

The second observed microstructural change was the growth of the infiltrated CGO particles. The initial CGO particle size before the test was in the range of 10 nm, as shown in Figure 11a as small bright dots homogeneously covering the Ni and YSZ grains. After the 1000 h long-term SOEC test at 800 °C the CGO microstructure changed significantly (Figure 11b). The CGO particles on the YSZ grains, seen as smaller bright dots in Figure 11b (marked with an ellipse), sintered and slightly grew compared to the initial microstructure (Figure 11a). The CGO particles on the Ni grains, as larger bright areas in Figure 11b (marked with a square), grew into large apparently dense Ce-containing layer on the Ni particles.

The chemical composition and crystal structure of the CGO layer on the YSZ grains and Ce-containing layer on the Ni grains were further investigated by TEM and the results are summarized in Figure 12. A bright-field TEM image of the fuel electrode of Cell B1 after 1000 h of testing is shown in Figure 12a. The STEM-EDS map presented in Figure 12b-c, where the Ni, YSZ and Ce-containing particles are represented by the Ni (red), Zr (blue) and Ce (green) Kα signals, confirms the observation by SEM (Figure 11) that the Ce-containing particles on Ni are larger than those on YSZ. The results of EDS spectra (presented as a line scan in Figure 12d) from the Ce-containing particles on the Ni surfaces showed that those also contained Gd, Al and O. The Ce-to-Al ratio is ca. 1 and the O-to-Ce ratio is ca. 3, obtained by quantifications of the EDS spectra. STEM-EDS maps of both Ce and Al signals (not presented) show that these elements are homogeneously distributed in the Ce-particle on the Ni

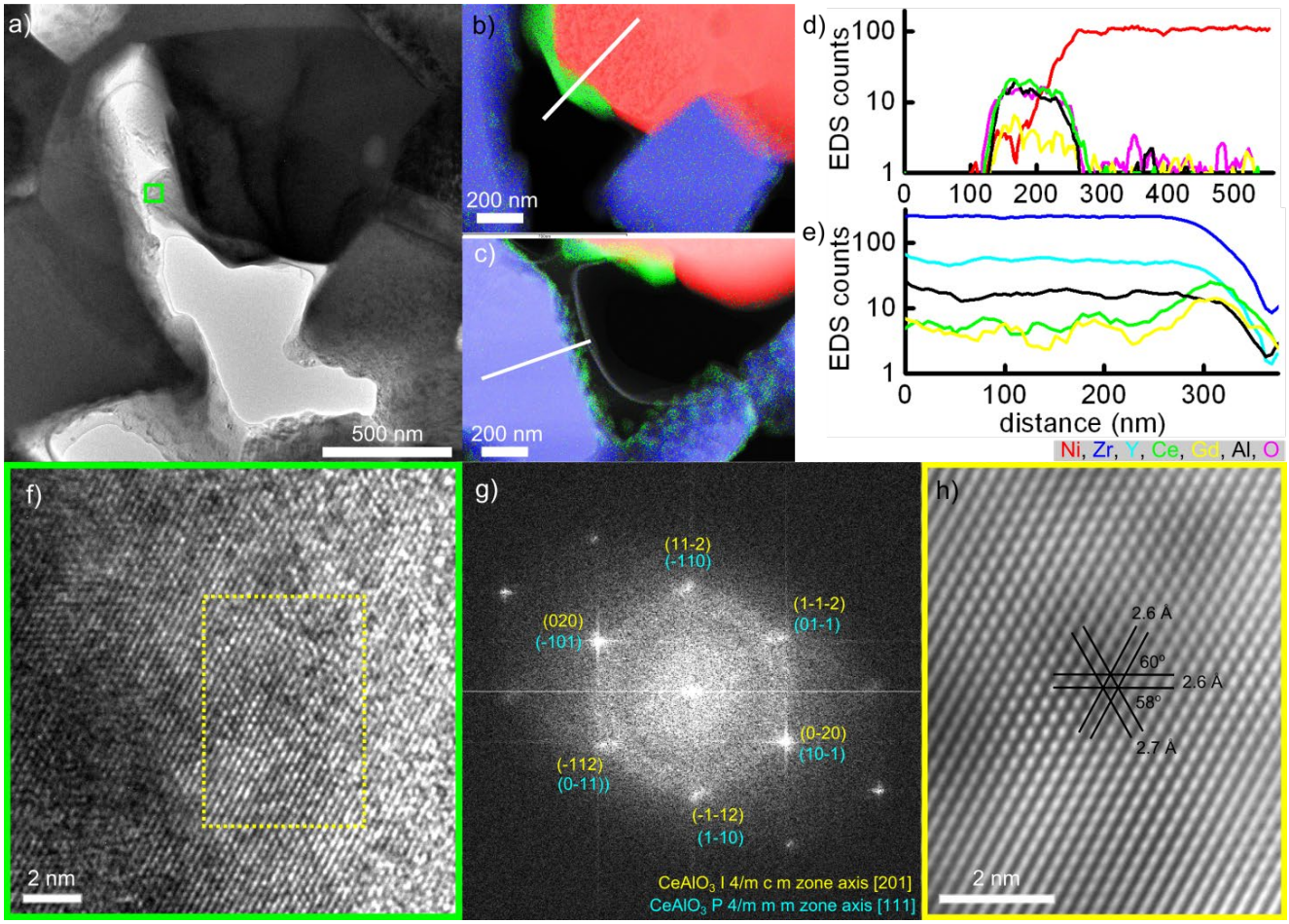

Figure 12: (a) Bright-field TEM image of an approximately 100 nm thin slice of the fuel electrode of Cell B1 after 1000 h of testing. (b) STEM-EDS map of the Ni Kα (red), Zr Kα (blue) and Ce Lα (green) X-ray signal overlaid with the a dark-field STEM image of approximately the same region of the sample as in (a). (c) STEM-EDS map of the Ni Kα (red), Zr Kα (blue) and Ce Lα (green) X-ray signal overlaid with the a dark-field STEM image (different region than in (c)). STEM-EDS line scans (d) from vacuum to a Ni particle and (e) from a YSZ particle to vacuum recorded from the regions marked by white lines in (b) and (c), respectively. The line scans present the X-ray signal from Ni Kα (red), Zr Kα (blue), Y Kα (cyan), Ce Lα (green), Gd Lα (yellow), Al Kα (black) and O Kα (magenta). (f) HRTEM image from the region marked by the green box in (a). (g) Fast Fourier transform (FFT) of (f). (h) An inverse FFT close-up from the region marked by the yellow box in (f) after masking out everything but the 6 indicated spots in (g). The result of the analysis of the HRTEM image (f) are presented as the identified crystal structure, zone axis and miller indices in (g) and measured lattice distances and angles in (h).

surfaces, which indicate that crystals of one composition with Ce, Al and O have formed, such as $CeAlO_3$. On most of the investigated YSZ surfaces, Ce and Gd were also observed as can be seen in Figure 12c and in the EDS line scan presented in Figure 12e. In the Ce-containing particles on the YSZ surface no or only a very weak signals from Al were detected. From the STEM images and EDS maps it can be seen that the Ce-Gd regions on the YSZ surface are present as relatively small particles. The formation of a similar thin Ce-rich particles on the YSZ surface has been reported, when samples were prepared by infiltration of Ce-nitrate solutions and calcination at high temperatures [53,54].

Measurements from the HRTEM image on one of the CGO particles on the Ni surface are consistent with the tetragonal $CeAlO_3$ crystal structure and with monoclinic ZrO_2, Figure 12f-h. Since, according to EDS analysis, this crystal is composed of Ce, Al, O, and Gd and not of Zr, the analysis suggests that the $CeAlO_3$ phase has formed. The HRTEM analysis does, however, not account for the presence of Gd. The TEM investigations suggest that all of CGO on the Ni surface was transformed into $CeAlO_3$ (most probably doped with Gd). This and other $CeAlO_3$ particle observed appeared to have a random orientation and no epitaxial growth on Ni grains was observed in HRTEM images or the selected area electron diffraction.

4. Discussion

4.1 Grain growth

Far smaller Ce-containing particles on the YSZ grains compared to those on the Ni grains after the SOEC test of 1000 h were observed in the CGO infiltrated Ni/YSZ electrode. Fuel electrodes operated in steam electrolysis are exposed to strong reducing conditions (cathodic polarization and hydrogen atmosphere). This can eliminate the self-limiting grain growth properties of Gd-doped ceria, which occurs through the solute drag effect, often reported for heat treatment of doped ceria in air [55–57]. In reducing conditions the grain boundary mobility is a function of the oxygen vacancies concentration and it is reported to be suppressed for a low dopant level and accelerated for a high dopant level [57]. Since a high dopant

level, 20 mol. % of Gd^{3+}, was used in the present study, it can be expected that the CGO grain growth self-limitation will be challenged and under the fuel electrode operation conditions the CGO particles will grow.

The more surprising finding is that the different surfaces of supporting grains influence the CGO grain growth differently. A similar difference in size of infiltrated CSO into a NiO/YSZ electrode has been reported by Zhang et al. for a short operation as SOFC, where the microstructural difference of CSO particles on the YSZ surface compared to those on the Ni surface was associated with different activity of the CSO particles [28]. However, a long heat treatment at 550 °C in reducing conditions of a CGO infiltrated Ni/YSZ backbone also resulted in larger CGO grains on the Ni surface than on the YSZ surface, as shown in Supplementary Information (Figure S4). From this it can be concluded, that the cathodic polarization cannot be the only explanation for the size difference observed in the here reported study. The explanation can lie in the Ni-ceria interface. The Ni-CeO_2 interface favors the dissociation of O-H bonds compared to the ceria surface at relatively low temperatures (25 – 350 °C) and that ceria can stabilize the Ni^{2+} species, as reported in Ref. [34]. Beside this, a direct contact between Ni and doped ceria greatly enhances the reduction of ceria under wet reducing conditions at 600 °C [35]. From this it can be speculated that the Ni-CGO interface has higher concentration of Ce^{3+} compared to the pure CGO and most probably also compared to the YSZ-CGO interface. The higher Ce^{3+} concentration can have two roles in the growth of Ce-containing particles: a) since size-wise Ce^{3+} is larger than Ce^{4+} and very similar to Gd^{3+}, the increased concentration of Ce^{3+} can unleash accelerated grain growth in CGO even at low temperatures or more likely b) it can facilitate formation of $CeAlO_3$, for which the growth rate can be significantly different than for CGO.

4.2 Steam electrolysis sites

Three different sites for the steam electrolysis on the CGO infiltrated Ni/YSZ electrode need to be considered: i) Ni/YSZ three phase boundary, ii) Ce-containing particles on the Ni grains and iii) CGO particles on the YSZ surface (Figure 13a). The Ni/YSZ three phase boundaries are the reaction sites where the electron percolating Ni network supplies electrons and the YSZ network provides an ion conductive path for oxide ions diffusing away from the reaction site (Figure 13a (I)). The number of Ni/YSZ TPB points is relatively small in a micrometer sized grain structure of the electrode. The infiltrated CGO network in the electrode can drastically increase the number of reaction sites, if the newly formed phases are active for the steam electrolysis (Figure 13a (II)). The CeO_2 – Ni model system has recently been studied for steam reduction reaction [34–36], showing that the CeO_2 – Ni interfaces can be crucial points for the steam reduction reaction. A thin Ce-containing layer on the YSZ support, presented in Figure 13a (III), has also been reported as a very efficient three-way-catalyst for the steam reduction reaction, especially due to high oxygen storage capacity and outstanding stable redox response upon oxidation and reduction treatments [53,54]. Based on these findings it cannot be ruled out that the steam electrolysis could occur on the

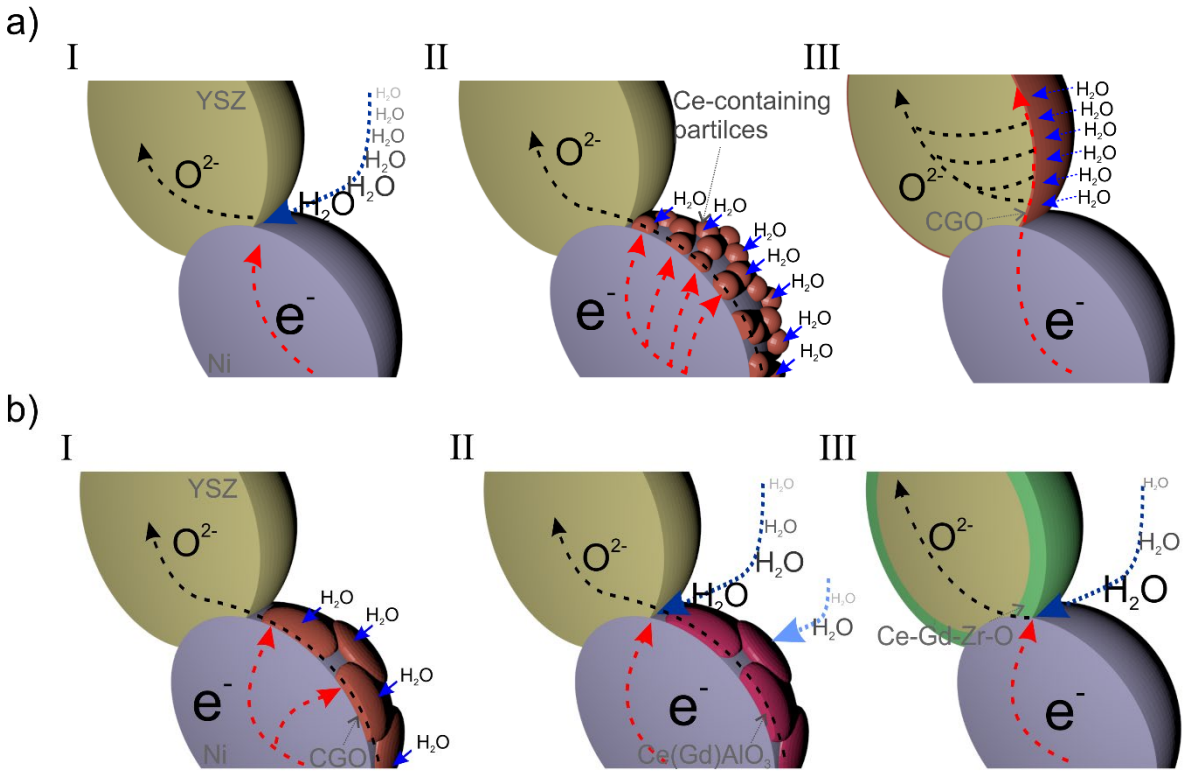

Figure 13: a) Schematic of possible stream reduction reaction sites (indicated with blue arrows): (I) at the Ni-YSZ TPB, (II) at the surface of CGO nanoparticles (small brown particles) supported on Ni grains and (III) at the CGO particles (thin brown layer) on the YSZ grains. b) Schematic of reaction sites for different degradation mechanisms: (I) growth of CGO nanoparticles, (II) formation of $CeAlO_3$ phase, (III) formation of insulating zirconate phase on YSZ grains. (the formation of H_2 in the scematics was omitted for easier interpretation). In the figure oxygen ion and the electron transport are indicated by black and red arrows, respectively.

Ce-containing particles on the Ni grains as well as on the Ce-containing particles on the YSZ grains. Even more, distinguishing which of these sites is preferential for the high temperature steam electrolysis is challenging. It can possibly change during operation, e.g. due to growth of CGO particles or formation of secondary phases (e.g. $CeAlO_3$) (Figure 13b).

4.3 Mechanism of the CGO infiltrated cell degradation

As presented in the TEM investigation in Figure 12, an Al-to-Ce ratio of ca. 1 was determined for the Ce-containing particles on the Ni grains, and the $CeAlO_3$ phase was identified. The Al in the Ni/YSZ electrode was introduced as a sintering aid [58,59] and it is present in both types of cells in the here reported study (in the bare Ni/YSZ electrodes and in the CGO infiltrated Ni/YSZ electrodes). However, its segregation was only observed on the CGO particles on Ni grains. The reported electrical conductivity of the $CeAlO_3$ phase measured in air at 800 °C is 0.006 S/cm [60] and it can be speculated that this is much lower than that of CGO at operating conditions of the cell (~0.10 S/cm at 800 °C and pO_2 of 10^{-15} atm. ~0.08 S/cm at 800 °C and pO_2 of 0.21 atm) [61]. The formation of the $CeAlO_3$ phase will slow down the electron and oxide ion transfer and thus the catalytic activity of the fuel electrode will be reduced (as schematically shown in Figure 13b (II)). This will mainly affect the polarization resistance of the cell, which was indeed increasing during long-term electrolysis of the CGO infiltrated cells (Cells B1 and B2). The difference in the degradation rate between two CGO infiltrated electrodes operating at steam conversion of 70 % and 42 % additionally point that the cell degradation can come from the formation of the $CeAlO_3$ phase. At high steam conversion, the Ni/YSZ electrode polarization will be larger, the interface pO_2 will be lower and consequently, the Ce^{3+} concentration will be higher. Hence, thermodynamically $CeAlO_3$ will form more easily.

Although the major contribution to the performance degradation most probably comes from the formation of $CeAlO_3$, it cannot be ruled out that a possible change of the Ce-containing particles on the YSZ surface can play a role for the cell performance. The Ce-containing particles on the YSZ support can form a secondary phase, although no identification of it was found in the here presented study (Figure 13b (III)). For a similar system, after exposure to temperatures higher than 1100 °C a pyrochlore phase was formed, which drastically reduced the activity of the catalyst [54].

Even though degradation was observed for the CGO infiltrated fuel electrodes, the drastic decrease of the degradation rate of the bare Ni/YSZ fuel electrode, shows the huge potential of using conventional solid oxide cells also for high current density electrolysis. The CGO infiltration, for drastic improvement of the cell performance, in the cell development scale represents an easy adoptable step, which can be fast scaled up and used also for the SOEC stack infiltration [31,32]. Even more, since the formation of $CeAlO_3$ is most probably the main degradation mechanism, omitting the Al_2O_3 sintering aid will drastically increase the durability of conventional solid oxide cells with the infiltrated CGO Ni/YSZ electrodes.

Conclusions

The SOEC performance degradation at high current densities (the rate of cell voltage increase) strongly depended on the microstructure and chemical composition of the fuel electrode. The CGO infiltration into the conventional Ni/YSZ fuel electrode drastically reduced the cell performance degradation tested at 800°C and -1.25 A/cm^2. For a cell with a bare Ni/YSZ fuel electrode the cell voltage increased with the rate of 699 mV/kh and for the cells with the CGO infiltrated Ni/YSZ fuel electrodes the rate was 66 mV/kh – 162 mV/kh. Contrary to the bare Ni/YSZ electrode, where a major microstructure degradation (loss of contact between Ni-YSZ particles, loss of contact between Ni-Ni particles and Ni particle migration away from the electrolyte) was observed, for the CGO infiltrated fuel electrode after the long-term electrolysis test only two microstructural changes were identified: i) Ni particle migration away from the electrolyte and ii) growth of infiltrated Ce-containing particles. No loss of contact between Ni-YSZ and Ni-Ni particles was observed. For the CGO infiltrated Ni/YSZ electrode three steam reduction sites have been proposed: Ni-YSZ TPB, CGO nanoparticles on the Ni grain surface and CGO nanoparticles on the YSZ grain surface, with the major degradation coming from the formation of a $CeAlO_3$ phase, which is formed by a reaction between Al from a sintering aid and the CGO particles on Ni grains. The lower degradation achieved in the CGO infiltrated Ni/YSZ electrode compared to the bare Ni/YSZ electrode shows high potential of the conventional cells for use in high current electrolysis applications.

Conflicts of interest

There are no conflicts to declare.

Acknowledgements

The authors gratefully acknowledge funding from Danish TSO – Energinet.dk through the project "Towards Solid Oxide Electrolysis Plants in 2020" (ForskEL 2015-1-12276). X. F. Tong acknowledges financial support from the China Scholarship Council (CSC). The authors are also grateful towards Xiufu Sun, Anne Hauch, Henrik Henriksen and Mahbooba Davodi for help with experimental work on the solid oxide electrolysis cell testing, Yi-Lin Liu for help with SEM images, and last but not least to Torben Jacobsen for help with fitting impedance spectra

Notes and references

1 W. A. Braff, J. M. Mueller and J. E. Trancik, *Nat. Clim. Chang.*, 2016, **6**, 964–969.
2 F. Klumpp, *J. Energy Storage*, 2016, **8**, 119–128.
3 M. Götz, J. Lefebvre, F. Mörs, A. McDaniel Koch, F. Graf, S. Bajohr, R. Reimert and T. Kolb, *Renew. Energy*, 2016, **85**, 1371–1390.
4 C. Graves, S. D. Ebbesen, S. H. Jensen, S. B. Simonsen and M. B. Mogensen, *Nat. Mater.*, 2014, **14**, 239–244.
5 M. Chen, Y.-L. Liu, J. J. Bentzen, W. Zhang, X. Sun, A. Hauch, Y. Tao, J. R. Bowen and P. V. Hendriksen, *J. Electrochem. Soc.*, 2013, **160**, F883–F891.
6 R. Knibbe, M. L. Traulsen, A. Hauch, S. D. Ebbesen and M. Mogensen, *J. Electrochem. Soc.*, 2010, **157**, B1209.

7 J. Kim, H.-I. Ji, H. P. Dasari, D. Shin, H. Song, J.-H. Lee, B.-K. Kim, H.-J. Je, H.-W. Lee and K. J. Yoon, *Int. J. Hydrogen Energy*, 2013, **38**, 1225–1235.

8 T. Wu, B. Yu, W. Zhang, J. Chen and S. Zhao, *RSC Adv.*, 2016, **6**, 68379–68387.

9 K. V. Hansen, M. Chen, T. Jacobsen, K. Thydén, S. B. Simonsen, S. Koch and M. B. Mogensen, *J. Electrochem. Soc.*, 2016, **163**, F1217–F1227.

10 Y. Zheng, J. Wang, B. Yu, W. Zhang, J. Chen, J. Qiao and J. Zhang, *Chem. Soc. Rev.*, 2017, **46**, 1427–1463.

11 S. Li, Y. Li, Y. Gan, K. Xie and G. Meng, *J. Power Sources*, 2012, **218**, 244–249.

12 L. Zhang, X. Zhu, Z. Cao, Z. Wang, W. Li, L. Zhu, P. Li, X. Huang and Z. Lü, *Electrochim. Acta*, 2017, **232**, 542–549.

13 Q. Liu, C. Yang, X. Dong and F. Chen, *Int. J. Hydrogen Energy*, 2010, **35**, 10039–10044.

14 X. Yue and J. T. S. Irvine, *J. Mater. Chem. A*, 2017, **5**, 7081–7090.

15 S. Ovtar, M. Chen, A. J. Samson and R. Kiebach, *Solid State Ionics*, 2017, **304**, 51–59.

16 D. Ding, X. Li, S. Y. Lai, K. Gerdes and M. Liu, *Energy Environ. Sci.*, 2014, **7**, 552.

17 K. Joong Yoon, M. Biswas, H.-J. Kim, M. Park, J. Hong, H. Kim, J.-W. Son, J.-H. Lee, B.-K. Kim and H.-W. Lee, *Nano Energy*, 2017, **36**, 9–20.

18 Y. Cheng, A. S. Yu, X. Li, T.-S. Oh, J. M. Vohs and R. J. Gorte, *J. Electrochem. Soc.*, 2016, **163**, F54–F58.

19 Y. Chen, Y. Zhang, Y. Lin, Z. Yang, D. Su, M. Han and F. Chen, *Nano Energy*, 2014, **10**, 1–9.

20 R. Kiebach, P. Zielke, S. Veltzé, S. Ovtar, Y. Xu, S. B. Simonsen, K. Kwok, H. L. Frandsen and R. Küngas, *J. Electrochem. Soc.*, 2017, **164**, F748–F758.

21 A. J. Samson, M. Sogaard, P. Hjalmarsson, J. Hjelm, N. Bonanos, S. P. V Foghmoes and T. Ramos, *Fuel Cells*, 2013, **13**, 511–519.

22 S. Ovtar, A. Hauch, S. Veltzé and M. Chen, *Electrochim. Acta*, 2018, **266**, 293–304.

23 L. Adijanto, R. Küngas, J. Park, J. M. Vohs and R. J. Gorte, *Int. J. Hydrogen Energy*, 2011, **36**, 15722–15730.

24 Y. Jin, H. Saito, K. Yamahara and M. Ihara, *Electrochem. Solid-State Lett.*, 2009, **12**, B8.

25 H. Shimada, E. Takami, F. Ohba, C. Takei, A. Hagiwara and M. Ihara, *J. Electrochem. Soc.*, 2011, **158**, B1341.

26 R. Fernández-González, J. C. Ruiz-Morales, J. Canales-Vázquez, J. R. Jurado, A. Makradi and P. Núñez, *Int. J. Hydrogen Energy*, 2016, **41**, 19731–19736.

27 S. P. Jiang, Y. Y. Duan and J. G. Love, *J. Electrochem. Soc.*, 2002, **149**, A1175.

28 L. Zhang, J. Gao, M. Liu and C. Xia, *J. Alloys Compd.*, 2009, **482**, 168–172.

29 W. Wang, S. P. Jiang, A. I. Y. Tok and L. Luo, *J. Power Sources*, 2006, **159**, 68–72.

30 J. Nielsen, T. Klemensø and P. Blennow, *J. Power Sources*, 2012, **219**, 305–316.

31 R. Kiebach, P. Zielke, J. V. T. Høgh, K. Thydén, H.-J. Wang, R. Barford and P. V. Hendriksen, *Fuel Cells*, 2016, **16**, 80–88.

32 T. L. Skafte, J. Hjelm, P. Blennow and C. Graves, *J. Power Sources*, 2018, **378**, 685–690.

33 W. C. Chueh, Y. Hao, W. Jung and S. M. Haile, *Nat. Mater.*, 2011, **11**, 155–161.

34 J. Carrasco, D. López-Durán, Z. Liu, T. Duchoň, J. Evans, S. D. Senanayake, E. J. Crumlin, V. Matolín, J. A. Rodríguez and M. V. Ganduglia-Pirovano, *Angew. Chemie Int. Ed.*, 2015, **54**, 3917–3921.

35 R. C. Maher, P. R. Shearing, E. Brightman, D. J. L. Brett, N. P. Brandon and L. F. Cohen, *Adv. Sci.*, 2016, **3**, 1500146.

36 V. Papaefthimiou, D. K. Niakolas, F. Paloukis, T. Dintzer and S. Zafeiratos, *ChemPhysChem*, 2017, **18**, 164–170.

37 M. Chen, X. Sun, C. Chatzichristodoulou, S. Koch, P. V. Hendriksen and M. B. Mogensen, *ECS Trans.*, 2017, **78**, 3077–3088.

38 S. D. Ebbesen, C. Graves, A. Hauch, S. H. Jensen and M. Mogensen, *J. Electrochem. Soc.*, 2010, **157**, B1419.

39 P. Hjalmarsson, X. Sun, Y.-L. Liu and M. Chen, *J. Power Sources*, 2013, **223**, 349–357.

40 H. Schichlein, A. C. Müller, M. Voigts, A. Krügel and E. Ivers-Tiffée, *J. Appl. Electrochem.*, 2002, **32**, 875–882.

41 S. H. Jensen, A. Hauch, P. V. Hendriksen, M. Mogensen, N. Bonanos and T. Jacobsen, *J. Electrochem. Soc.*, 2007, **154**, B1325.

42 A. Hauch, K. Brodersen, M. Chen and M. B. Mogensen, *Solid State Ionics*, 2016, **293**, 27–36.

43 S. Primdahl, *J. Electrochem. Soc.*, 1998, **145**, 2431.

44 S. Primdahl, *J. Electrochem. Soc.*, 1999, **146**, 2827.

45 C. Graves, RAVDAV data analysis software, (2012).

46 K. Thydén, Y. L. Liu and J. B. Bilde-Sørensen, *Solid State Ionics*, 2008, **178**, 1984–1989.

47 S.B. Simonsen, CrystalMatch, (2016). http://www.staff.dtu.dk/sobrs/Software.

48 S. H. Jensen, A. Hauch, P. V. Hendriksen and M. Mogensen, *J. Electrochem. Soc.*, 2009, **156**, B757.

49 H. Monzón and M. A. Laguna-Bercero, *Electrochim. Acta*, 2016, **221**, 41–47.

50 M. H. Pihlatie, A. Kaiser, M. Mogensen and M. Chen, *Solid State Ionics*, 2011, **189**, 82–90.

51 J. Nielsen and J. Hjelm, *Electrochim. Acta*, 2014, **115**, 31–45.

52 M. B. Mogensen, A. Hauch, X. Sun, M. Chen, Y. Tao, S. D. Ebbesen, K. V. Hansen and P. V. Hendriksen, *Fuel Cells*, 2017, **17**, 434–441.

53 M. P. Yeste, J. C. Hernández-Garrido, D. C. Arias, G. Blanco, J. M. Rodríguez-Izquierdo, J. M. Pintado, S. Bernal, J. A. Pérez-Omil and J. J. Calvino, *J. Mater. Chem. A*, 2013, **1**, 4836.

54 C. Arias-Duque, E. Bladt, M. A. Muñoz, J. C. Hernández-Garrido, M. A. Cauqui, J. M. Rodríguez-Izquierdo, G. Blanco, S. Bals, J. J. Calvino, J. A. Pérez-Omil and M. P. Yeste, *Chem. Mater.*, 2017, **29**, 9340–9350.

55 P.-L. Chen and I.-W. Chen, *J. Am. Ceram. Soc.*, 1994, **77**, 2289–2297.

56 P.-L. Chen and I.-W. Chen, *J. Am. Ceram. Soc.*, 1996, 79, 1793–1800.

57 D. W. Ni, D. Z. de Florio, D. Marani, A. Kaiser, V. B. Tinti and V. Esposito, *J. Mater. Chem. A*, 2015, **3**, 18835–18838.

58 P.H. Larsen, K. Brodersen, Method for the manufacture of reversible solid oxide cells, 8790847, 2007.

http://patents.justia.com/patent/8790847.
59 B. Charlas, D. W. Ni, H. L. Frandsen, K. Brodersen and M. Chen, *Fuel Cells*, 2017, **17**, 132–143.
60 A. I. Shelykh and B. T. Melekh, *Phys. Solid State*, 2003, **45**, 248–252.
61 I. Navarro, F. Marques and J. Frade, *J. Electrochem. Soc.*, 1997, **144**, 267–273.